Journal of Colloid and Interface Science 636 (2023) 646–656

Contents lists available at ScienceDirect

Journal of Colloid and Interface Science

journal homepage: www.elsevier.com/locate/jcis

Z-scheme WOx/Cu-g-C_3N_4 heterojunction nanoarchitectonics with promoted charge separation and transfer towards efficient full solar-spectrum photocatalysis

Xiao Zhang [a], Katarzyna Matras-Postolek [a,*], Ping Yang [b,*], San Ping Jiang [c,*]

[a] Faculty of Chemical Engineering and Technology, Cracow University of Technology, Krakow, Poland
[b] School of Material Science & Engineering, University of Jinan, Jinan 250022, PR China
[c] WA School of Mines: Mineral, Energy and Chemical Engineering, Curtin University, Perth, WA 6845, Australia

GRAPHICAL ABSTRACT

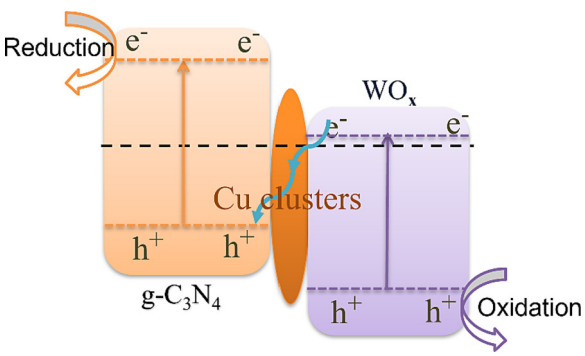

ARTICLE INFO

Article history:
Received 27 September 2022
Revised 7 January 2023
Accepted 11 January 2023
Available online 13 January 2023

Keywords:
g-C_3N_4
Nanosheets
Cu nanoparticles
H_2 evolution
CO_2 reduction

ABSTRACT

Construction of Z-scheme heterojunctions has been considered one superb method in promoting solar-assisted charge carrier separation of carbon-based materials to achieve efficient utilization of solar energy in hydrogen production and CO_2 reduction. One interesting concept in nanofabrication that has become trend recent years is nanoarchitectonics. A heterostructure photocatalyst constructed based on the idea of nanoarchitectonics using the combination of g-C_3N_4, metal and an additional semiconducting nanocomposite is investigated in this paper. Z-scheme tungsten oxide incorporated copper modified graphitic carbon nitride (WO_x/Cu-g-C_3N_4) heterostructures are fabricated via immobilization of WO_x on Cu nanoparticles modified superior thin g-C_3N_4 nanosheets. Mechano-chemical pre-reaction and a two-step high-temperature thermal polymerization process are the keys in attaining homogeneous distribution of Cu nanoparticles in g-C_3N_4 nanosheets. The horizontal growth of homogeneously distributed WO_x nanobelts on Cu modified g-C_3N_4 (Cu-g-C_3N_4) base via solvothermal synthesis is achieved. The photocatalytic performances of the heterostructures are evaluated through water splitting and CO_2 photoreduction measurements in full solar spectrum irradiation condition. The presence of Cu nanoparticles in the composite system improves charge transport between g-C_3N_4 and WO_x and thus enhances the photocatalytic performances (H_2 generation and CO_2 photoreduction) of the composite material, while the presence of WO_x nanocomposites enhances light absorption of the composite material in the near infrared range. The synthesized heterostructure with optimized WO_x to Cu-g-C_3N_4 ratio and in case of no co-catalyst addition exhibits enhanced photocatalytic H_2 evolution (4560 $\mu mol g^{-1} h^{-1}$) as well as excellent CO_2 reduction rate (5.89 $\mu mol g^{-1} h^{-1}$ for CO generation).

* Corresponding authors.
E-mail addresses: k.matras@pk.edu.pl (K. Matras-Postolek), mse_yangp@ujn.edu.cn (P. Yang), S.Jiang@curtin.edu.au (S. Ping Jiang).

https://doi.org/10.1016/j.jcis.2023.01.052
0021-9797/© 2023 The Authors. Published by Elsevier Inc.
This is an open access article under the CC BY license (http://creativecommons.org/licenses/by/4.0/).

© 2023 The Authors. Published by Elsevier Inc. This is an open access article under the CC BY license (http://creativecommons.org/licenses/by/4.0/).

1. Introduction

Solar-assisted chemical fuel production has been receiving growing attention recent years due to the rising global energy demand and escalating climate crisis [1–5]. Topics such as conversion of CO_2 and water into valuable fuels using semiconducting photocatalysts has been extensively studied, particularly, the conversion of solar energy to hydrogen energy via water splitting [6–10]. One of the major challenges confronted in developing catalysts with high light-harvesting ability for a variety of photocatalytic applications is the utilization of solar energy over broad spectral range, especially in the visible (Vis) to near-infrared (NIR) range (which constitutes about 90 % of the solar energy) [11].

For completing overall water splitting reaction to generate O_2 and H_2, the valence band maximum of the photocatalyst has to be more positive than the oxidation potential of water (O_2/H_2O, 1.23 V vs normal hydrogen electrode (NHE)), and the conduction band minimum needs to be more negative than the reduction potential of H^+/H_2 (0 V vs NHE). Moreover, efficient separation and transport of the photogenerated charge carriers plays the key role in enhancing hydrogen evolution performance of the catalyst [12–14]. In case of CO_2 reduction for valuable carbon-based fuel (methane, methanol, ethylene etc.) production, compared with electrocatalytic CO_2 reduction, photocatalytic CO_2 reduction is advantaged by its applicability under ambient temperature and pressure [15–17]. Semiconductor photocatalysts have been widely exploited in H_2 generation and CO_2 photoreduction applications [18,19]. The construction of semiconducting heterostructure photocatalysts with enhanced charge separation and transport efficiency has been drawing great attention [20–22], particularly, the development of heterostructures with suitable band gaps, enhanced interfacial properties and high solar energy conversion efficiency [23–25].

Metal-free graphitic carbon nitride (g-C_3N_4) has been given considerable attention in the application of photocatalytic solar-to-fuels conversion in recent years due to its high stability, electronic band structure, visible-light responsiveness, low-cost and nontoxicity nature [26,27]. A variety of approaches have been investigated to enhance charge separation and transport in g-C_3N_4 including metal and non-metal doping, morphology adjustment, and construction of heterostructural composites. Particularly, superior thin two-dimensional (2D) g-C_3N_4, as a carbon-based 2D layered substrate material with large surface area, has been considered a great option for constructing g-C_3N_4-based heterostructures [28]. Highly conductive metals (Ag, Au, Cu) have been considered excellent options for modifying g-C_3N_4 attaining enhanced photocatalytic performances, because these metal atoms incorporated into the heptazine-based π-conjugated system of layered g-C_3N_4 are able to improve the in-plane charge transport in the composite system. Moreover, the presence of abundant N sites in g-C_3N_4 nanosheets also favours metal incorporation in g-C_3N_4 [29]. Although plenty of research works has been done on metal incorporation in g-C_3N_4, especially in noble metal modification of layered g-C_3N_4 nanosheets [30], to achieve homogeneous distribution of these metal particles is still not easy. It is thus imperative to develop novel photocatalysts with homogeneously distributed metal particles for controlled photocatalytic oxidation and reduction processes.

Due to the poor electron affinity and high stability of CO_2 molecules, the sluggish kinetics of CO_2 reduction reaction, particularly the C=O bond dissociation reactions (with a dissociation energy of higher than 750 kJ/mol), is the main cause of the requirement of a substance (catalyst, photosensitizer) that can facilitate CO_2 conversion [31,32]. The energy required for photocatalytic CO_2 conversion facilitated by the presence of a photocatalyst (with improved photogenerated electron-hole separation and migration efficiency) is much lower than that required for direct C=O bond dissociation. Photocatalysis utilizing semiconducting heterostructure photocatalysts, has been one promising approach to perform efficient CO_2 photoreduction [33,34]. The built-in electric field developed within semiconducting heterostructures facilitates charge separation and migration, leading to improved catalyst surface reaction efficiency and catalytic activity [35–40]. Transition metal nanocomponents involving tungsten oxides are commonly used for modification of g-C_3N_4 to construct g-C_3N_4-based type II heterostructures. For instance, g-C_3N_4 nanosheets based layered heterostructures with horizontally grown WO_x nanobelts have been examined to have excellent photocatalytic performances under visible and NIR light irradiation due to extended light absorption range [15]. WO_{3-x} nanorods modified g-C_3N_4 nanosheets based heterostructures have been reported to have enhanced CO_2 photoreduction activity [41]. Despite of the efficient separation of photogenerated charge carriers in type II heterostructures, the redox abilities of the photogenerated electrons and holes on the reaction sites of these heterostructures are in most of the cases relatively weak. Construction of multicomponent heterostructural composites (e.g., type II, S-scheme, Z-scheme heterostructure system) with improved charge carrier separation efficiency and high redox ability are thus needed. Nanoarchitectonics has been one of the novel concepts in nanofabrication that has become trend recent years. The basic idea of nanoarchitectonics is the construction of multifunctional nanomaterial by combining and coupling different functional nanomaterials and nanostructures [5,9]. Z-scheme heterostructure photocatalysts constructed using the combination of g-C_3N_4, noble metal (Cu) and semiconducting nanocomposite (WO_x) is studied in this paper.

In general, a photocatalytic Z-scheme heterostructure system involves a two-step photoexcitation process that efficiently separates the photogenerated charge carriers and improves the redox performance of the catalyst material. To date, a variety of g-C_3N_4 based Z-scheme heterostructure composites with enhanced photoinduced charge carrier separation efficiency has been developed [38,42] Noble metal (Pd, Au, Pt, Cu) loaded Z-scheme heterostructures are hot choices in attaining improved H_2 generation, owing to the low overpotential observed in the catalyst system and the enhanced charge separation achieved via facilitated transport of photogenerated electrons in the conduction band of g-C_3N_4 [30,32]. The photoinduced electrons in the catalyst system can be transported across the metal–semiconductor interface due to the Schottky effect, resulting in enhanced photogenerated charge carrier separation and improved catalytic activities. For instance, Pd nanoparticles modified g-C_3N_4 composites were reported to have outstanding catalytic activity for room-temperature Suzuki-Miyaura coupling reaction [43]. Moreover, the interfacial charge transport and electronic structure of g-C_3N_4 nanosheets can be modulated by the formation of Z-scheme heterostructures via incorporation of noble metal nanoparticles to improve the photocatalytic activities of the heterostructures. However, to achieve homogeneous dispersion of metal nanoparticles in g-C_3N_4 and modulated interfacial charge transport in semiconducting

nanocomponents incorporated Z-scheme heterostructures for attaining high H_2 generation and CO_2 reduction efficiency can be challenging.

As a relatively low-cost noble metal, copper and copper base composite materials have been widely exploited in electrocatalysis, particularly in selective CO_2 reduction [44]. The Cu (1 0 0) facet is generally favourable to C_2H_4 generation (from CO_2 reduction) at relatively low overpotential, while Cu (1 1 1) facet favours CH_4 production [44]. To improve the photocatalytic performance of copper base composites, extending light absorption range and increasing photogenerated charge carrier separation and transport efficiency are imperative. In this paper, a novel approach utilizing the combination of mechano-chemical pre-reaction and thermal condensation processes at high temperature condition was developed for treating superior thin g-C_3N_4 nanosheets with Cu nanoparticles to enhance charge carrier separation and transport efficiency of the composite system. A solvothermal synthetic process was used to incorporate WO_x on the Cu-g-C_3N_4 nanosheets to create the 2D/2D WO_x/Cu-g-C_3N_4 layered Z-scheme heterostructures (as illustrated in Scheme 1) with extended light adsorption in NIR region. The photocatalytic mechanism of these Z-scheme heterostructures were studied utilizing various techniques involving transmission electron microscopy (TEM), X-ray photoelectron spectroscopy (XPS), X-ray diffraction (XRD), and Raman spectroscopy etc. The heterostructures synthesized using optimized preparation conditions showed enhanced CO_2 photoreduction performances with a CO evolution rate of 6.8 $\mu molg^{-1}h^{-1}$ and a CH_4 generation rate of 3.2 $\mu molg^{-1}h^{-1}$.

2. Experimental section

2.1. Chemicals and preparation of Cu modified g-C_3N_4

Chemicals used (with no further purification) for the preparation and characterization of the samples including melamine (99 %), copper (II) acetylacetonate ($Cu(acac)_2$, 97 %), ethanol (99 %), triethanolamine (99 %), ascorbic acid (AA, 99 %), and WCl_6 (99.99 %) were purchased from Sigma Aldrich. For comparison uses, pure ultrathin g-C_3N_4 nanosheets (CN in Table 1) with no copper addition was synthesized using a two-step calcination method reported in one of our preliminary works [21]. Cu modified g-C_3N_4 (Cu-g-C_3N_4) was prepared via a combination of mechano-chemical pre-reaction and two-step thermal polymerization processes (using high temperature setting). Bulk g-C_3N_4 (as the substrate material) was synthesized via thermal polymerization at 500 °C using melamine as the precursor. To construct Cu-g-C_3N_4, a mixture of certain amount of $Cu(acac)_2$, 2 g of bulk g-C_3N_4 and ethanol were ground to dry before undergoing thermal treatment in tube furnace. For instance, 0.5, 1.0, and 1.5 wt% of $Cu(acac)_2$ in 2 g of g-C_3N_4 was used to obtain the Cu modified g-C_3N_4 sample Cu-CN-1, Cu-CN-2, and Cu-CN-3, respectively (with detailed preparation conditions used for each sample listed in Table 1). Thermal polymerization process was then carried out in an inert atmosphere at 700 °C for 2 h using a ramp rate of 5 °C/min. To test the effects of the mechano-chemical pre-reaction process on the samples, a Cu modified g-C_3N_4 sample (named as Cu-CN-4 in Table 1) synthesized using similar processes as other Cu-g-C_3N_4 samples but via no mechano-chemical pre-reaction was also fabricated.

2.2. Preparation of WO_x/Cu-g-C_3N_4 heterojunctions

WO_x incorporated Cu modified g-C_3N_4 (WO_x/Cu-g-C_3N_4) heterojunctions were fabricated using sample Cu-CN-2 as the base. To verify the effects of tungsten source on the heterojunction formation, different weight percentage of WCl_6 (as the tungsten source) was added to a mixture containing ethanol and 0.8 g of sample Cu-CN-2 followed by 5 min of sonication treatment. 6.0, 8.0, and 10.0 wt% of WCl_6 were treated with the Cu-CN-2 base to obtain the WO_x incorporated Cu modified g-C_3N_4 composite sample W-Cu-CN-1, W-Cu-CN-2, and W-Cu-CN-3, respectively (Table 1). Scarce amount of AA was added (with the molar ratio of WCl_6 to AA been 1:1) to ensure the presence of oxygen vacancies in WO_x. 20 min of stirring was required before heat treatment at 220 °C for 10 h. The products were washed several times with ethanol before freeze drying. For comparison, WO_x incorporated composite samples using sample Cu-CN-4 as the base were also prepared (named as W-Cu-CN-4 in Table 1).

2.3. Characterization

Material characterization: To investigate the morphology of the WO_x/Cu-g-C_3N_4 samples, transmission electron microscope (TEM) (FEI Titan G2 80–200 TEM/STEM) was used to collect TEM images and HAADF-STEM images of the samples. X-ray diffractometer (Bruker D8) and Kratos AXIS Ultra DLD spectrometer were utilized to collect X-ray diffraction (XRD) patterns and X-ray photoelectron spectroscopy (XPS) spectra of the samples. UV–vis diffuse reflectance and absorbance spectra of the WO_x/Cu-g-C_3N_4

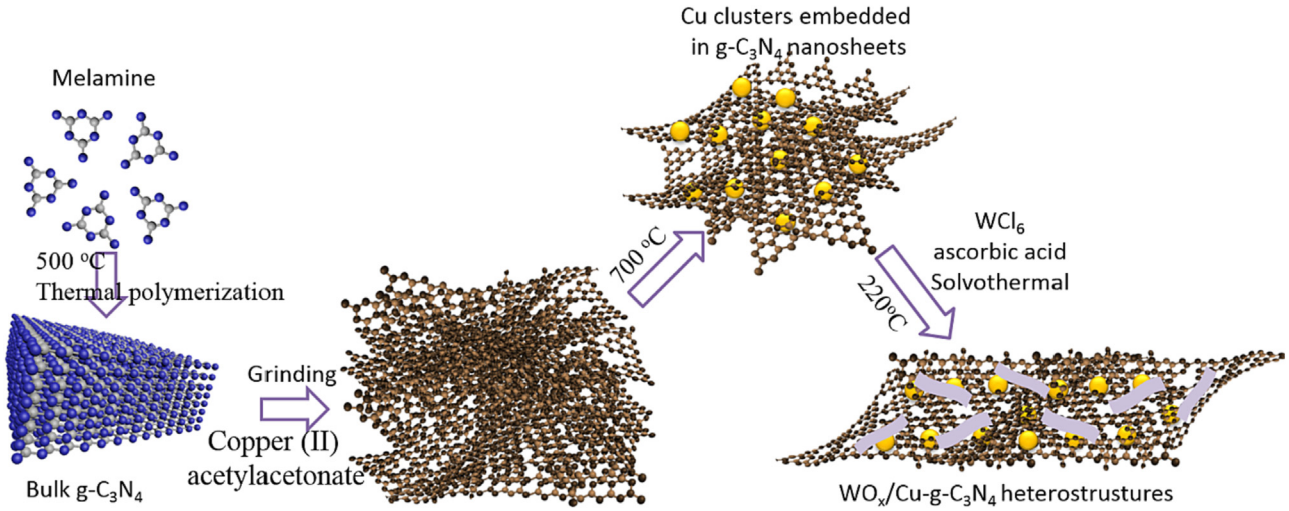

Scheme 1. Formation mechanism of WO_x/Cu-g-C_3N_4 heterostructures.

Table 1
Sample preparation conditions.

Sample	Composition	$Cu(acac)_2$ (wt %)*	WCl_6 (wt %)**	Procedure
CN	g-C_3N_4	0	0	Two-step calcination
Cu-CN-1	Cu-g-C_3N_4	0.5	0	Pre-reaction
Cu-CN-2	Cu-g-C_3N_4	1.0	0	Pre-reaction
Cu-CN-3	Cu-g-C_3N_4	1.5	0	Pre-reaction
Cu-CN-4	Cu-g-C_3N_4	1.0	0	No pre-reaction
W-Cu-CN-1	WO_x/Cu-g-C_3N_4	0.5	6.0	Pre-reaction
W-Cu-CN-2	WO_x/Cu-g-C_3N_4	1.0	8.0	Pre-reaction
W-Cu-CN-3	WO_x/Cu-g-C_3N_4	1.5	10.0	Pre-reaction
W-Cu-CN-4	WO_x/Cu-g-C_3N_4	1.0	8.0	No pre-reaction

* Weight ratio percentage of $Cu(acac)_2$/melamine during preparation.
** Weight ratio percentage of WCl_6/Cu-g-C_3N_4 used for preparation.

samples were also recorded using UV–vis spectrophotometer (U-4100, Hitachi).

Photocatalytic characterization: Photocatalytic H_2 evolution measurements was performed on samples using a testing system with glass-closed gas circulation and Pyrex top-irradiation reaction vessels. Mixture containing 10 mg of the composite sample and 100 mL of triethanolamine solution (with triethanolamine to deionized water ratio of 1:9) was used for sample testing. 25 min of sonication and degassing (to remove air in the reaction vessel system) were done on samples before light exposure. A 300 W Xe arc lamp was used as the light source. The amount of H_2 evolved was measured via gas chromatography (Shimadzu GC-7920) using Ar as the carrier gas. To estimate the experimental error, repeated measurements (3 times) were also done on the samples. Sample solution for photocatalytic CO_2 reduction test was prepared using 20 mg of the WO_x/Cu-g-C_3N_4 sample and 15 mL of deionized water. 15 min of high-purity CO_2 bubbling was done on the sample solution before CO_2 reduction measurements. A 300 W Xe lamp was used as the light source while GC-7920 gas chromatograph was used to analyze the gases generated during measurements. The photocatalytic rhodamine B (RhB) degradation performances of the samples were also evaluated using 10 mg/l RhB solution and a 300 W Xe arc lamp equipped with wavelength cut-off filters as the light source (800 nm and 420–760 nm filters were used for NIR and Vis irradiation, respectively).

Similar procedures as RhB photodegradation measurements except for the addition of scavengers were used to investigate the active species in photocatalytic process under full spectrum irradiation condition. 0.0216 g of Benzoquinone (BQ), 2 mL isopropanol (IPA), 0.034 g of $AgNO_3$, and 0.0744 g of Ethylenediaminetetraacetic acid disodium salt (EDTA-Na_2) in 35 mL of sample photocatalyst dispersed RhB solution was used as the scavengers for superoxide radicals ($\bullet O_2^-$), hydroxyl radicals ($\bullet OH$) electrons (e^-), and holes (h^+), respectively. The electron spin resonance (ESR) signals of hydroxyl and superoxide radical adducts of 5,5-dimethyl-1-pyrroline-*N*-oxide (DMPO) were collected using Bruker model ER200-SRC spectrometer (under full spectrum irradiation condition).

3. Results and discussion

The bulk g-C_3N_4 nanosheets utilized as the base precursor was obtained via thermal polymerization of melamine at 500 °C. A mechno-chemical pre-reaction process was required to treat bulk g-C_3N_4 with copper (II) acetylacetonate before calcination at 700 °C, as illustrated in Scheme 1. In general, ideal g-C_3N_4 nanosheets are composed of melem building blocks involving tri-s-triazine (C_6N_7) and triazine (C_3N_3) units [25–29]. In the π-conjugated system of layered g-C_3N_4 base consisting of nitrogen and sp^2 hybridized carbon, the abundant N sites worked as the key reaction sites for anchoring Cu atoms on g-C_3N_4 during the thermal polymerization process [29]. The mechanical grinding process before thermal polymerization treatment was crucial for forming Cu incorporated g-C_3N_4 composites via nucleation and growth of Cu nanoparticles on ultrathin g-C_3N_4 nanosheets. And a 220 °C solvothermal treatment method was utilized to immobilize WO_x on Cu modified g-C_3N_4. The detailed experimental condition used for sample preparation are listed in Table 1.

The TEM images of the Cu modified g-C_3N_4 composites (sample Cu-CN-1, Cu-CN-2, and Cu-CN-3) are shown Fig. 1a to 1c. Superior thin nanosheet morphology was observed for all three samples. Homogeneously distributed small Cu nanoparticles (with diameters less than 4 nm) can be observed on the TEM images. The amount of Cu nanoparticles formed in the Cu-g-C_3N_4 composite system increases as the the amount of Cu source (copper (II) acetylacetonate) added increases (as observed for sample Cu-CN-1, Cu-CN-2, and Cu-CN-3). An enlarged TEM image of sample Cu-CN-3 showing a typical layered structure with clear Cu lattice fringes confirming the successful incorporation of Cu nanoparticles in g-C_3N_4 nanosheets is shown in Fig. S1 in the Supporting Information section. The lattice spacing of 0.22 nm measured in the insets in Fig. 1a to 1c corresponds to the lattice fringes of Cu (1 1 1) facet. The lattice spacing estimated (0.22 nm) coincide well with that measured for pristine Cu nanoparticle (0.21 nm) reported in literature [45], and this can be ascribed to the incorporation of g-C_3N_4 substrate in the composite system. To examine the role of mechano-chemical pre-reaction process in the distribution of Cu in the composites system, sample Cu-CN-4 was prepared with no mechano-chemical pre-reaction treatment. Chunky Cu particles were observed as shown in the TEM images of sample Cu-CN-4 (see Fig. S2 in Supporting Information). Fig. 1d to 1f shows the TEM images of sample W-Cu-CN-2. The fiber-like darker area on Fig. 1e and 1f can be associated with the WO_x nanobelts incorporated in the W-Cu-CN-2 heterostructures as they are similar to the WO_x nanobelts observed in sample W-Cu-CN-3 (in Fig. 1g to 1i). An enlarged image of the darker area in Fig. 1f are shown in Fig. S3 (see Supporting Information). The lattice spacing measured in Fig. S3 matched with the spacing of g-C_3N_4. The TEM images of sample W-Cu-CN-3 are shown in Fig. 1g to 1i. As the amount of W source (WCl_6) added increased, the amount of WO_x nanobelts formed along the surface of Cu-g-C_3N_4 nanosheets also increased. The lattice spacing of 0.38 nm measured in the nanobelts area in Fig. 1i corresponds to the (0 1 0) facet of WO_3.

The elemental mappings of the composite samples before and after WO_x immobilization on Cu-g-C_3N_4 nanosheets (sample Cu-CN-2 and W-Cu-CN-2) were recorded and are shown in Fig. 2. As shown in Fig. 2a, except for a few evident Cu chunky nanoparticle area observed, the distribution of Cu in most of the randomly selected scanned area was quite homogeneous. This indicates that the Cu incorporated in sample Cu-CN-2 are mostly in the small nanoparticle form. Completely homogeneously distributed C and N elements were observed for both sample Cu-CN-2 and W-Cu-

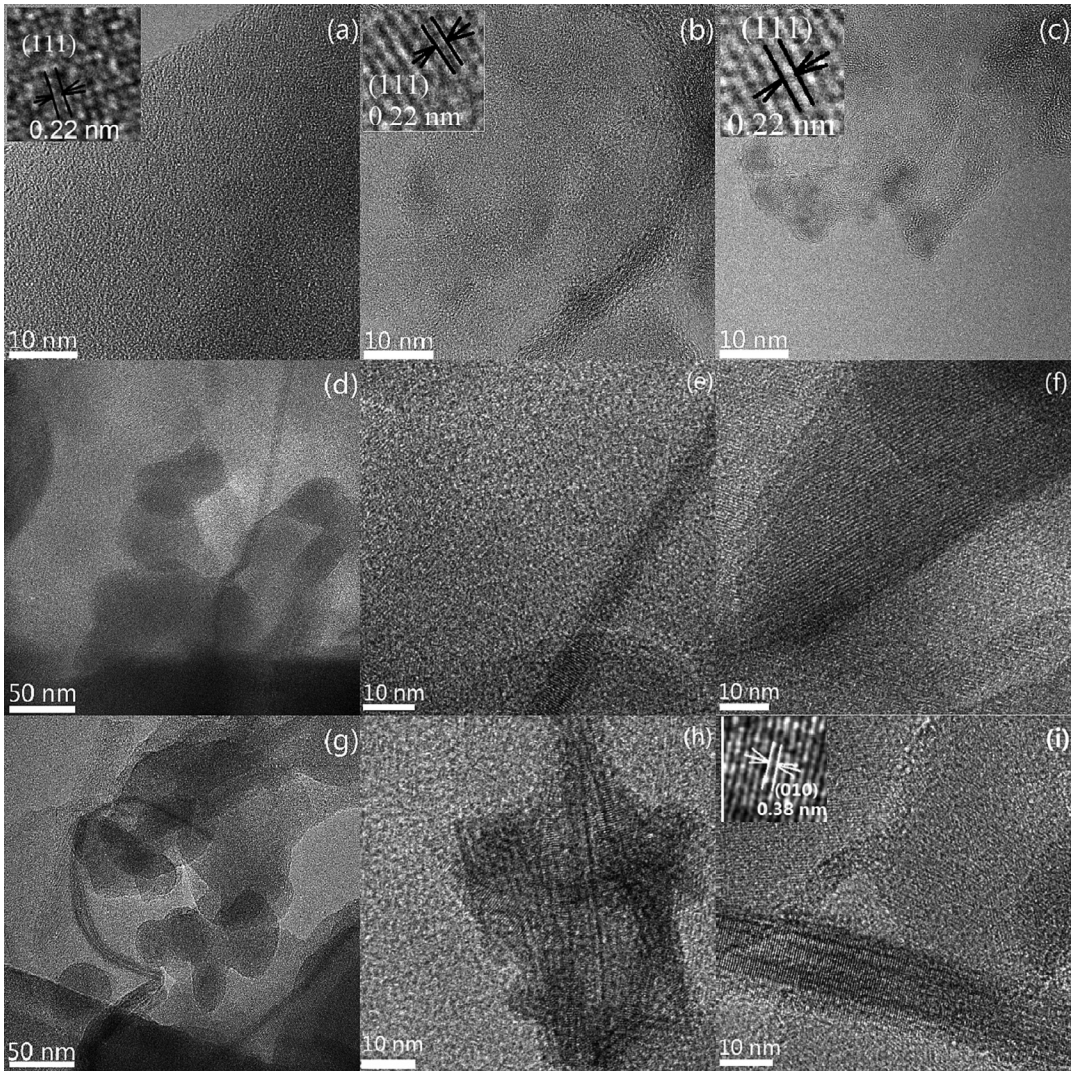

Fig. 1. TEM images of g-C_3N_4 and heterostructures: (a) Cu-CN-1; (b) Cu-CN-2, (c) Cu-CN-3; (d to f) W-Cu-CN-2; (g to i) W-Cu-CN-3. The insets in (a) to (c) are enlarged Cu nanoparticles area with a lattice spacing of 0.22 nm corresponding to the Cu (1 1 1) facet. The inset in (i) shows the lattice fringes of WO_x with a spacing of 0.38 nm corresponding to the (0 1 0) facet of WO_x.

CN-2 (Fig. 2c, 2b, 2e, and 2f). The HADDF-STEM image of sample W-Cu-CN-2 (prepared using sample Cu-CN-2 as the base material) is shown in Fig. 1d. The distribution of Cu on sample W-Cu-CN-2 (shown in Fig. 2g) was much more homogeneous than those on sample Cu-CN-2, which can be attributed to the secondary diffusion process of Cu during the solvothermal synthesis stage [7]. The fiber-like aggregates observed in W and O mappings in Fig. 2h and 2i are due to the formation of WO_x nanobelts in the heterostructure, which also matched with the WO_x nanobelts area observed on the HADDF-STEM image (Fig. 2d). The presence of W an O elements in the whole specimen area (in Fig. 2h and 2i) confirms the presence of WO_x across the whole Cu-g-C_3N_4 nanosheets area. In addition, the successful incorporation of W and Cu into the W-Cu-CN-2 composites system was also confirmed by using TEM energy dispersive X-ray spectroscopy (EDS) analysis (see Fig. S4 in Supporting Information).

According to the XPS spectra collected for sample W-Cu-CN-2 shown in Fig. 3, the four main peaks observed in the C 1 s spectrum in Fig. 3a corresponded to the O-C=O (289.1 eV), C—N/C=O (288.4 eV), C-OH (286.3 eV), and C—C (284.7 eV) peaks. The N 1 s spectrum in Fig. 3b has three main peaks corresponding to the graphitic N (401.0 eV), pyridinic N (398.7 eV), and pyrrolic N (399.8 eV) peak; as well as two π excitation peaks at 406.2 and 404.5 eV. The pyridinic N is the key N active sites on the heterostructure that promotes nucleation of WO_x in the composites system. The O 1 s spectrum in Fig. 3c was fitted into three peaks at 532.9, 531.3, and 530.2 eV, corresponding to the organics/H_2O, hydroxide, and oxide peaks, respectively. The peaks observed at 35.4 and 37.3 eV in Fig. 3d can be attributed to W4$f_{7/2}$ and W 4$f_{5/2}$ of W^{6+} state, while the peaks at 33.9 and 36.4 eV are attributed to the W^{5+} state [38]. The presence of W^{5+} and W^{6+} states of WO_x confirmed the presence of oxygen vacancies in the WO_x/Cu-g-C_3N_4 heterostructure system. The oxygen vacancy defects can be considered one of the key factors that promotes the separation of photogenerated charge carriers of WO_x incorporated catalysts thus enhancing the photocatalytic performances of the catalysts. The sharp and symmetrical Cu 2p peaks observed at 932.4 and 952.5 eV in Fig. 3e corresponded to the Cu $2p_{3/2}$ and Cu $2p_{1/2}$ peaks. And these peaks can be indexed to Cu(0) [42,43], owing to the fact that the characteristic peaks of Cu(I) often have strong satellite features around 936 eV and within the 940 ~ 950 eV range [44,45].

The XRD patterns recorded for sample Cu-CN-2, Cu-CN-3, W-Cu-CN-2 and W-Cu-CN-3 (Fig. 4a) illustrated that the diffraction

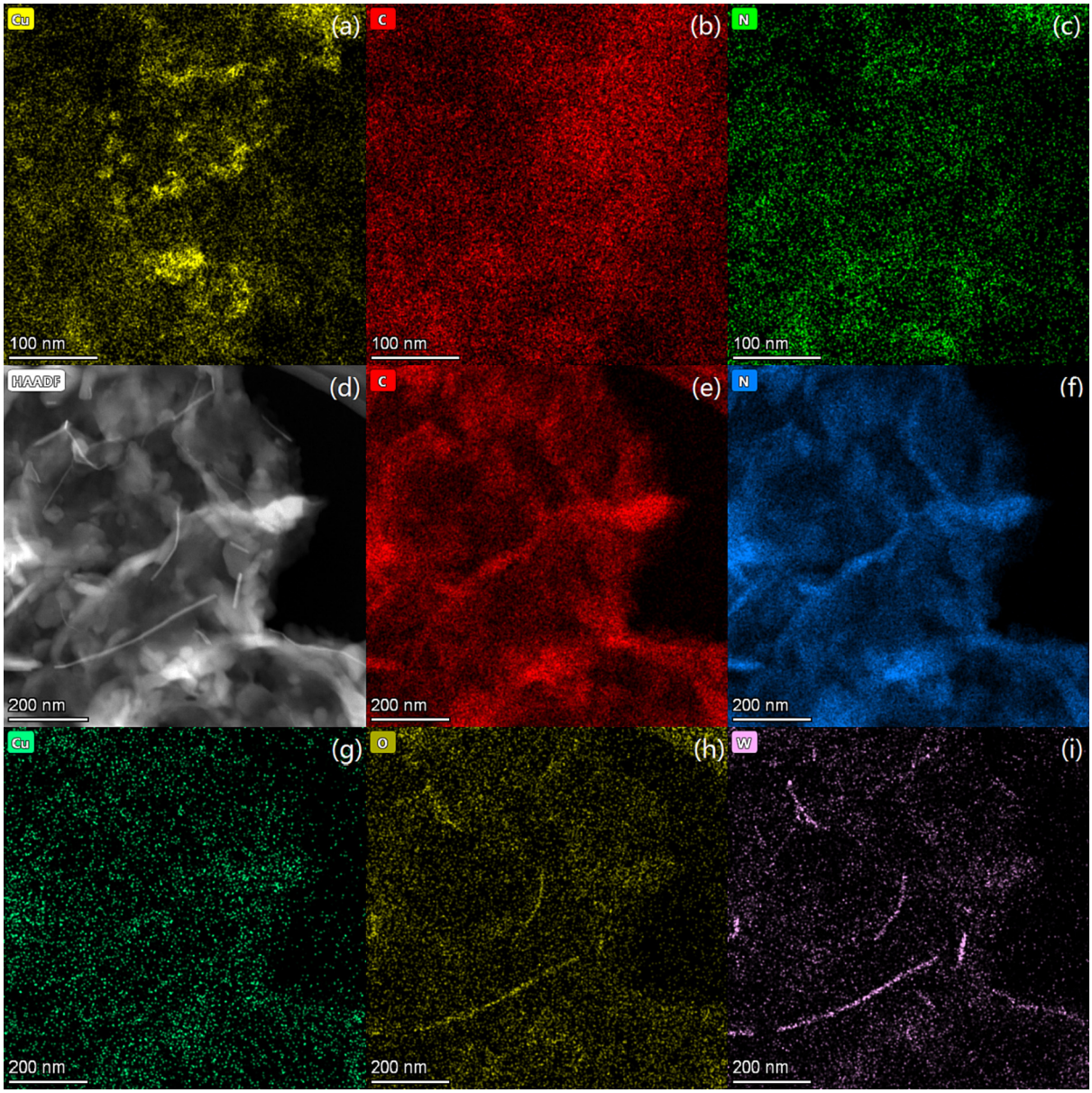

Fig. 2. (a to c) Elemental mapping of sample Cu-CN-2: (a) Cu; (b) C; and (c) N. (d to i) HADDF image. Elemental mapping of sample W-Cu-CN-2: (e) C; (f) N; (g) Cu; (h) O; and (i) W.

peaks corresponding to the (100) and (002) facets of g-C_3N_4 were observed in all four samples. Due to the incorporation of WO_x in the Cu-g-C_3N_4 composites system, peak shift (towards larger angle) occurred for the most intense peak (that are associated with the stacking of conjugated system of g-C_3N_4) in the WO_x immobilized samples, from 27.8° for sample Cu-CN-2 to 27.9° for sample W-Cu-CN-2, as shown in Fig. 4b. The XRD pattern of sample W-Cu-CN-2 in Fig. 4a consists of peaks of both WO_2 and WO_3 phases, suggesting the existence of both two phases in the highly crystalline Cu-g-C_3N_4 based WO_x composites. The presence of WO_2 phase peak (in Fig. 4a) is due to the use of reducing agent during the solvothermal synthesis stage, indicating successful incorporation of defects-engineered WO_x in the composites system. Moreover, the weak peak intensities observed for the WO_x components also demonstrated that the amount of WO_x incoporated in sample W-Cu-CN-2 and W-Cu-CN-3 was relatively low.

The UV laser excited Raman spectra of sample CN, Cu-CN-2, and W-Cu-CN-2 were collected for microstructure comparison (Fig. 4c). Sample CN showed a typical Raman spectrum of g-C_3N_4 with relatively weakened peak intensity, confirming the successful formation of layered g-C_3N_4 via the two-step calcination process. However, an increase in g-C_3N_4 related peak intensity was observed after Cu nanoparticle immobilization. This can be attributed to the effects of copper on thermal polymerization. The mechano-chemical pre-reaction treatment (of copper source and g-C_3N_4 precursors before thermal polymerization) was the key that causes Cu ions been able to enter the g-C_3N_4 network easily, creating a Cu immobilized g-C_3N_4 composite with highly ordered nanostructure. Moreover, the Raman peaks recorded for sample W-Cu-CN-2 were similar to that for sample Cu-CN-2, suggesting that the relatively ordered unit arrangement and nanostructure of Cu modified g-C_3N_4 nanosheets were able to be maintained after solvothermal treatment. In comparison with the Raman peaks of pristine g-C_3N_4 nanosheets (sample CN), the relatively intense peak observed in the 800–1000 cm^{-1} range (marked using asterisk symbol in Fig. 4c) confirms the interplay among g-C_3N_4, Cu, and

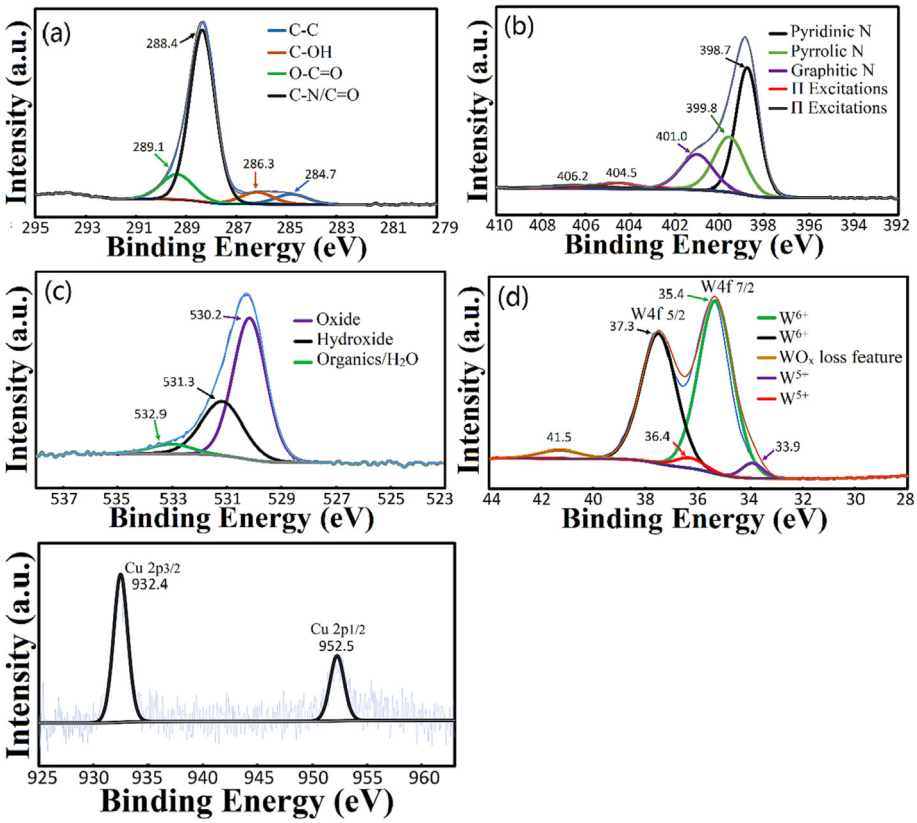

Fig. 3. XPS spectra of sample W-Cu-CN-2: (a) C1s spectrum; (b) N1s spectrum; (c) O1s spectrum; and (d) W4f spectrum; (e) Cu 2p spectrum.

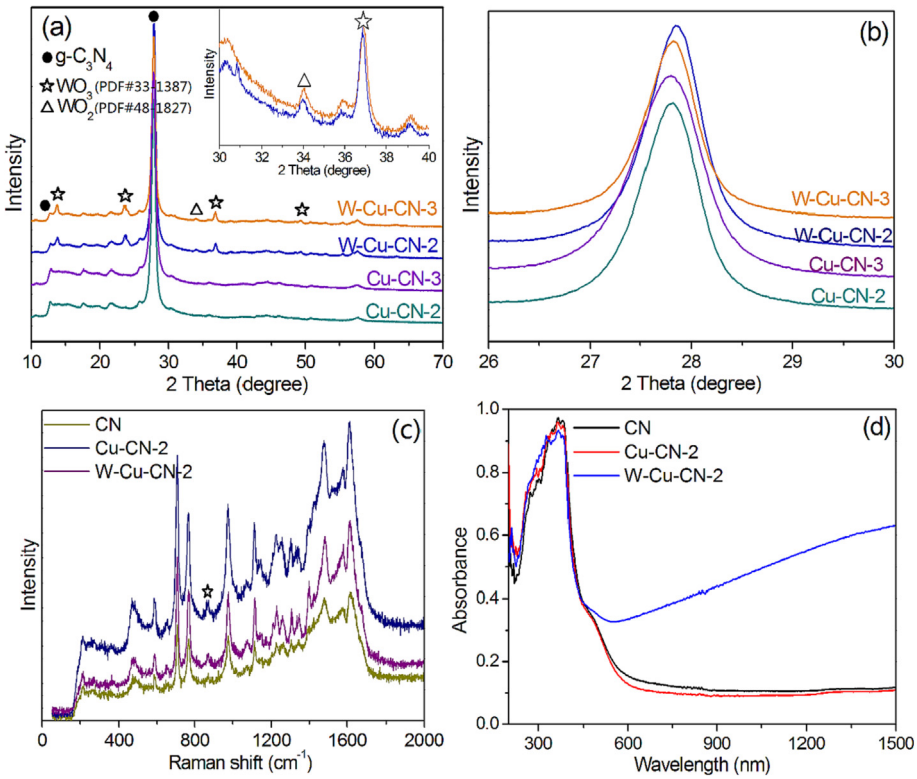

Fig. 4. (a & b) XRD patterns of the samples. (c) UV–vis diffuse reflectance spectra of the samples. (d) Raman spectra of the samples. The inset in (a) shows the XRD patterns of sample W-Cu-CN-2 and W-Cu-CN-3 in the 30 ~ 40° range.

WO_x in the heterostructure. The UV–vis diffuse reflectance spectra of sample CN, Cu-CN-2, and W-Cu-CN-2 (Fig. 4d) shows that the diffuse reflectance spectrum of the sample remained almost unchanged only after Cu modification. A drastic change in the spectrum was observed after WO_x incorporation, enhanced visible and near infrared absorption was observed for the WO_x modified sample (W-Cu-CN-2), which can be attributed to the band gap narrowing and decreased band-to-band excitation energy [46]. The extended light absorption to the full solar spectrum range resulted in significant enhancement in photocatalytic performances.

Photocatalytic hydrogen evolution and CO_2 photo-reduction measurements were done on the samples under full solar spectrum condition without the addition of co-catalysts. The results are shown in Fig. 5 and Table 2. Cu-CN-2 showed the highest H_2 generation activity (0.62 $mmolg^{-1}h^{-1}$) among the Cu modified g-C_3N_4 (Cu-CN) samples. The H_2 generation rate (in case of no co-catalysts addition) obtained for sample W-Cu-CN-1, W-Cu-CN-2, and W-Cu-CN-3 were 2.99, 4.56, and 3.49 $mmolg^{-1}h^{-1}$, respectively. The amount of H_2 evolved from WO_x incorporated Cu-g-C_3N_3 composites was significantly higher than their Cu-g-C_3N_4 base counterparts. In comparison with the H_2 generation rate measured for sample W-Cu-CN-4 (synthesized with no mechano-chemical pre-treatment, 2.75 $mmolg^{-1}h^{-1}$), sample W-Cu-CN-2 showed a much higher efficiency of 4.56 $mmolg^{-1}h^{-1}$ that is about 7.35 times of that of sample Cu-CN-2 (which is also higher than most of the WO_x modified g-C_3N_4 composites reported in literature) [15,41,47]. These indicate that the addition of WO_x and mechano-chemical pre-treatment process, as well as the control of the amount of Cu incorporated into the composites system are the key factors that causes drastic enhancement in H_2 evolution efficiency. In addition, the photocatalytic measurements in NIR light irradiation condition were also performed to further examine the role of WO_x nanocomposites in the heterostructure system. The H_2 evolution rate of sample W-Cu-CN-2 under NIR light irradiation was 1.78 $mmolg^{-1}h^{-1}$, and almost no H_2 evolution was observed for sample Cu-CN-2. This also confirms that the extended light absorption range in the NIR region (owing to the presence of WO_x nanobelts) is one of the keys to photocatalytic performance enhancement of heterostructures. The cyclic stability data in Fig. 5b shows that sample W-Cu-CN-2 also revealed excellent stability in photocatalytic H_2 generation as the evolution rate remained almost unchanged after 5 cycles of measurements. To further examine the change in crystal phase and in WO_x component after photocatalysis measurements, XRD data were collected for the used sample (sample after 20 cycles of H_2 evolution measurements). The XRD analysis shows that no obvious WO_2 XRD peak was observed, which can be attributed to the oxidizing of WO_x by the photoinduced holes that leads to diminishing or disappearing of oxygen vacancies.

Table 2
H_2, CO, and CH_4 evolution rate obtained for the samples (under full solar spectrum).

Sample	H_2 (mmol/g/h)	CO (μmol/g/h)	CH_4 (μmol/g/h)
CN	0.25	n/a	n/a
Cu-CN-1	0.48	0.30	0.27
Cu-CN-2	0.62	0.52	0.33
Cu-CN-3	0.56	0.48	0.30
Cu-CN-4	0.24	n/a	n/a
W-Cu-CN-1	2.99	3.78	1.65
W-Cu-CN-2	4.56	5.89	2.31
W-Cu-CN-3	3.48	4.35	1.78
W-Cu-CN-4	2.75	1.08	0.89

In order for photocatalytic overall water splitting involving the oxygen evolution reaction (also called the water oxidation reaction, eq. (1)) and hydrogen evolution reaction (proton reduction, eq. (2)) to occur, the band gap of the photocatalyst has to be larger than 1.23 V, specifically, the valence band maximum of the photocatalyst needs to be more positive than the oxygen evolution potential (0.82 V vs NHE at pH = 7, eq. (1)), and the conduction band minimum of the photocatalyst is required to be more negative than the proton reduction potential (-0.41 V vs NHE, at pH = 7, eq. (2)) [48,49].

$$H_2O + 2\ h^+ \rightarrow O_2 + 2H^+ + 4e^- \quad E^0 = 0.82\ V\ vs\ NHE \tag{1}$$

$$2H^+ + 2e^- \rightarrow H_2 \quad E^0 = -0.41\ V\ vs\ NHE \tag{2}$$

In general, loading of metal co-catalyst is often required for improving hydrogen evolution efficiency because these metal co-catalysts are pivotal to trapping photogenerated charge carriers and promoting charge transport as well as suppressing the recombination of charge carriers. However, in the case of the WO_x incorporated Cu modified g-C_3N_4 (W-Cu-CN) heterostructure, no additional co-catalysts were required since Cu worked perfectly as the charge carrier trapping site in this case.

CO_2 photoreduction (CO and CH_4 evolution) tests were also performed on the samples and the data are listed in Table 2. In case of photocatalytic CO_2 conversion, the conduction band minimum of the photocatalyst has to be more negative than the standard carbon-based fuel (e.g., CO, CH_3OH, CH_4 etc. generated from CO_2 reduction reaction) evolution potential (-0.24 V vs NHE at pH = 7 for CH_4 generation, eq. (3); −0.52 V for CO generation, eq. (4)) [49,50].

$$CO_2 + 8H^+ + 8e^- \rightarrow CH_4 + 2H_2O \quad E = -0.24\ V \tag{3}$$

$$CO_2 + 2H^+ + 2e^- \rightarrow CO + H_2O \quad E = -0.52\ V \tag{4}$$

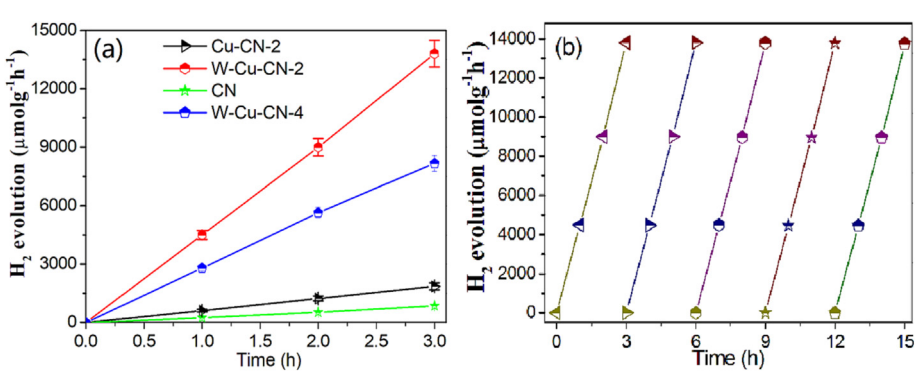

Fig. 5. (a) H_2 generation activity plot (with error bars) of the samples under xenon lamp irradiation (full spectrum) with no co-catalyst addition. (b) Time courses of photocatalytic H_2 evolution on sample W-Cu-CN-2 (for five cycles in 15 h).

Sample W-Cu-CN-2 exhibited higher CO (5.89 μmolg^{-1}h^{-1}) and CH_4 (2.31 μmolg^{-1}h^{-1}) evolution efficiency than that of the other WO_x incorporated Cu-g-C_3N_4 composites (W-Cu-CN-1, W-Cu-CN-3, W-Cu-CN-4) and the Cu modified g-C_3N_4 samples. Similar trend was also observed for the H_2 evolution measurements. No CO and CH_4 were evolved in case of using pristine g-C_3N_4 nanosheets (sample CN). Among the Cu modified g-C_3N_4 samples, Cu-CN-2 showed the best CO (0.52 μmolg^{-1}h^{-1}) and CH_4 (0.33 μmolg^{-1}h^{-1}) evolution rate. The incorporation of WO_x into the Cu-g-C_3N_4 base system is the key in improving CO_2 photoreduction efficiency of the heterostructure composites. As expected, the photocatalytic performances of sample Cu-CN-4 and W-Cu-CN-4 (synthesized with no mechano-chemical pre-treatment) were not satisfactory.

Construction of multicomponent semiconductor photocatalysts with narrowed band gap and extended light absorption range (to absorb greater proportions of solar spectrum) based on the idea of nanoarchitectonics, can be pivotal to improving photocatalytic performance of the catalyst material. WO_x with suitable bandgap, abundant surface oxygen vacancies and localized surface plasmon resonance (LSPR) property shows a broad absorption in the Vis and NIR region [38]. The presence of abundant oxygen vacancies in tungsten oxide causes collective oscillations of free charges, which is also similar to that of the LSPR phenomenon observed in noble metals. The three electron transition pathways under solar light irradiation proposed for the nonstoichiometric WO_x (possessing abundant oxygen vacancies) are illustrated in Scheme 2a, involving direct electron excitation from valence band to conduction band; electron transition from valence band to the energy states associated with oxygen vacancies; and transition caused by LSPR excitation. By creating extra charge carrier transport pathways in the composite material (with conduction band and oxygen vacancies working as the electron traps), the charge carrier transport efficiency was improved and enhancement in photocatalytic performance was achieved.

To further investigate the photocatalytic mechanism and active species of WO_x incorporated Cu-g-C_3N_4 composites, quenching experiments aimed at identifying active species for rhodamine B (RhB) degradation and electron spin resonance (ESR) measurements were done on sample W-Cu-CN-2 (Fig. 6 and Fig. S5 in Supporting Information). EDTA-Na_2, BQ, IPA, and $AgNO_3$ were used as scavengers of h^+, •O^{2-}, •OH, and e^-, respectively. The result shows that RhB photodegradation was significantly inhibited by the addition of BQ, indicating •O^{2-} to be the main active species for RhB degradation in this case. The ESR spin-trap test was performed on sample W-Cu-CN-2 using DMPO as the nitrone-type spin trap agent for detecting DMPO-radical adducts generated in water (DMPO-•O^{2-}) and in methanol (DMPO-•OH). As shown in Fig. 6, no adduct signal was observed in dark condition, signals of both DMPO-•O^{2-} and DMPO-•OH adducts were observed only under light irradiation. It is thus confirmed that the •O^{2-} and •OH are two major active species generated in the WO_x/Cu-g-C_3N_4 heterostructure assisted photocatalysis process. The photocatalytic •OH (eq. (5)) and •O^{2-} (eq. (6)) generation reactions are shown below [49].

$$OH^- + h^+ \rightarrow \bullet OH,\ 2.7\ \text{V, vs NHE} \tag{5}$$

$$O^2 + e^- \rightarrow \bullet O^{2-},\ -0.046\ \text{V, vs NHE} \tag{6}$$

Since the O^2/•O^{2-} potential of −0.046 V is more positive than the conduction band minimum of g-C_3N_4 but more negative than the conduction band minimum of WO_x, pristine WO_x is incapable of generating •O^{2-} under light irradiation condition. However, according to the ESR analysis, •O^{2-} and •OH were demonstrated to be the active species generated in the WO_x/Cu-g-C_3N_4 photocatalytic system. Thus, the WO_x/Cu-g-C_3N_4 composites photocatalyst does not adapt to the conventional type II heterojunction structure. Instead, the WO_x/Cu-g-C_3N_4 composites showed a direct solid-state Z-scheme charge transport pathway as illustrated in Scheme 2b (with the position of conduction and valance band estimated based on the Tauc plots and XPS valence-band spectra data reported in our previously published papers and in literature) [25,27,36,41,44,51,52]. Since the photogenerated electrons transport from the conduction band of WO_x to the valence band of g-C_3N_4 (Scheme 2b) in this case, the WO_x/Cu-g-C_3N_4 Z-scheme photocatalytic system with improved spatial separation of photogenerated charge carriers and suppressed electron-hole pair recombination is beneficial for facilitating redox reactions and improving photocatalytic activity. The incorporation of Cu nanoparticles in the heterostructure system and the integration of WO_x in the g-C_3N_4 hybrid heterostructure are pivotal to to band gap narrowing and light absorption enhancement, resulting in significantly improved photocatalytic activity of the constructed Z-scheme WO_x/Cu-g-C_3N_4 photocatalyst. In addition, the presence of homogeneously incorporated Cu nanoparticles is also beneficial for enhancing the conductivity of the heterostructures and facilitating charge migration in the heterostructure system. Moreover, since the Cu (1 1 1) surface has excellent binding abilities to H_2O and CO_2, H_2O-assisted CO_2 photoreduction on Cu (1 1 1) surface can be achieved via the dissociation of CO_2 into *CO intermediate followed by hydroxy-methylidyne intermediate (*C-OH) formation via *CO reduction. The *C-OH intermediate is crucial in facilitating photocatalytic CO_2 reduction reaction since this intermediate can be reduced and hydrogenated for producing carbon-based fuels. For example, methane can be generated from *C intermediate formation (via *C-OH reduction) followed by the hydrogenation process, while ethylene can be produced through *C-OH hydrogenation (forming *CH_2 intermediate) and dimerization process.

In case of Z-scheme WO_x/Cu-g-C_3N_4 heterostructures, the charge carriers generated from the photocatalytic system migrate quickly through Cu nanoparticles to g-C_3N_4 to achieve enhanced charge carrier separation. Meanwhile, the photo-excited electrons generated from WO_x (exhibiting LSPR property) are imperative to facilitating photocatalytic reactions. As a metal oxide with relatively high work function, WO_x with abundant oxygen vacancy is able to create extra charge transport paths in Z-scheme heterostructure system to enhance charge carrier transport. The built-in electric field developed at the interface of WO_x and g-C_3N_4 facilitates interfacial charge carrier separation and transport and improves the photocatalytic activity of WO_x/Cu-g-C_3N_4 heterostructure composites.

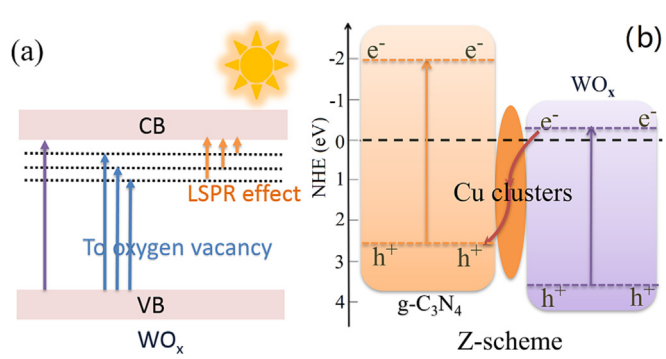

Scheme 2. Schematic diagram of electron transition pathways in WO_x (a) and photocatalytic mechanism of Z-scheme photocatalytic system for WO_x/Cu-g-C_3N_4 composites (b).

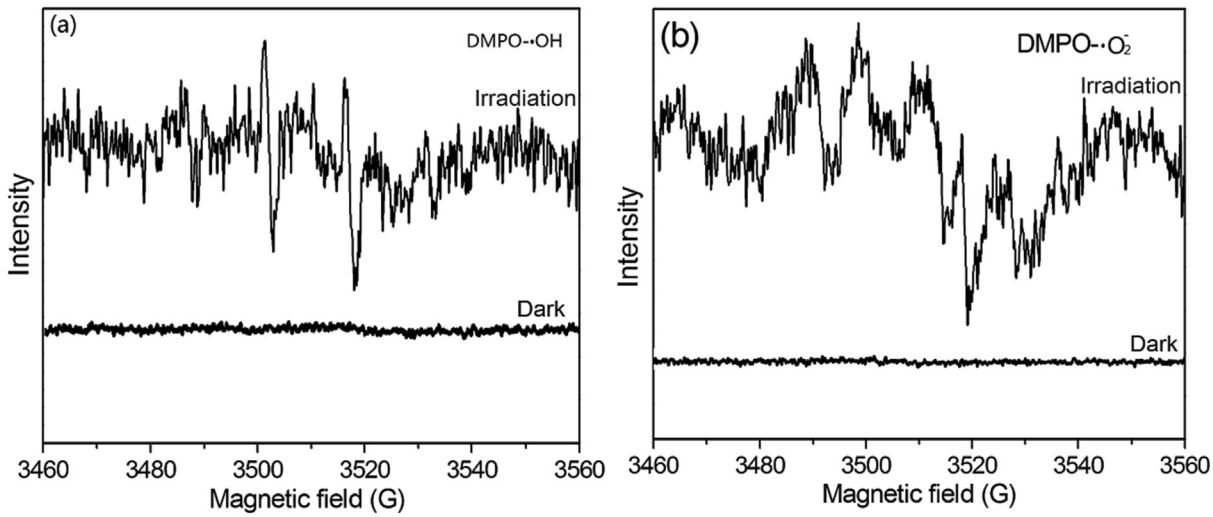

Fig. 6. DMPO spin-trapping ESR spectra of sample W-Cu-CN-2: (a) recorded in aqueous solution for DMPO-•OH adduct under light irradiation; and (b) in methanol solvent for DMPO-•O_2^- adduct.

4. Conclusions

Z-scheme WO_x/Cu-g-C_3N_4 heterostructures with enhanced photocatalytic performance under full solar spectrum irradiation condition were constructed based on the idea of nanoarchitectonics using a mechano-chemical pre-reaction assisted two-step thermal polymerization method with relatively high temperature settings. The homogeneous distribution of Cu nanoparticles in the ultrathin g-C_3N_4 nanosheets plays the key role in improving the photocatalytic performance of the heterostructure composites. The H_2 generation (4560 $\mu molg^{-1}h^{-1}$) and CO_2 photoreduction performance of the constructed WO_x/Cu-g-C_3N_4 composites were significantly improved even in case of no co-catalyst addition. The optimized preparation parameters of the WO_x/Cu-g-C_3N_4 composites are the keys in enhancing CO_2 photoreduction efficiency (with a CO generation rate of 5.89 $\mu molg^{-1}h^{-1}$ and a CH_4 evolution rate of 2.31 $\mu molg^{-1}h^{-1}$) of the composite material, which is also much higher than that of WO_x modified g-C_3N_4 composites [15,41]. The improved photocatalytic activity of WO_x/Cu-g-C_3N_4 composites are due to the synergistic effects in-between the three components in the heterostructure system--WO_x nanocomposites, Cu nanoparticles and g-C_3N_4 nanosheets. Moreover, the incorporation of Cu nanoparticles in the composites system resulted in enhanced charge transport and increased conductivity (as well as improved catalytic activity) of the WO_x/Cu-g-C_3N_4 composites, while the presence of WO_x nanocomposites in the heterostructure system was the key to the extended light absorption range (to visible and NIR region) and enhanced photocatalytic performances of the material. This work offers a novel strategy for constructing heterostructures with enhanced catalytic activity by incorporating Cu nanoparticles into ultrathin g-C_3N_4 nanosheets providing a better understanding of interactions between metal nanoparticles and the g-C_3N_4 matrix in a composite system, especially for developing layered ultrathin g-C_3N_4 nanosheets based multicomponent photocatalysts in full-spectrum solar fuel conversion application.

CRediT authorship contribution statement

Xiao Zhang: Conceptualization, Data curation, Formal analysis, Methodology, Writing – original draft. **Katarzyna Matras-Postolek:** Methodology, Project administration. **Ping Yang:** Formal analysis, Methodology, Writing – review & editing. **San Ping Jiang:** Formal analysis, Methodology, Writing – review & editing.

Data availability

No data was used for the research described in the article.

Declaration of Competing Interest

The authors declare that they have no known competing financial interests or personal relationships that could have appeared to influence the work reported in this paper.

Acknowledgements

This research is part of the project No. 2021/43/P/ST5/01729 co-funded by the National Science Centre and the European Union Framework Programme for Research and Innovation Horizon 2020 under the Marie Skłodowska-Curie grant agreement No. 945339 . For the purpose of Open Accesss, the author has applied a CC-BY public copyrght license to any Author Accepted Manuscript (AAM) version arising from this submission.

Appendix A. Supplementary material

Supplementary data to this article can be found online at https://doi.org/10.1016/j.jcis.2023.01.052.

References

[1] Y. Wang, X. Wang, M. Antonietti, Polymeric graphitic carbon nitride as a heterogeneous organocatalyst: from photochemistry to multipurpose catalysis to sustainable chemistry, Angew. Chem. Int. Ed. 51 (2012) 68–89, https://doi.org/10.1002/anie.201101182.
[2] J. Ran, M. Jaroniec, S.Z. Qiao, Cocatalysts in semiconductor-based photocatalytic CO_2 reduction: achievements, challenges, and opportunities, Adv. Mater. 30 (2018) 1704649, https://doi.org/10.1002/adma.201704649.
[3] Z. Jiang, X. Zhang, J. Wang, L. Chen, H.S. Chen, P. Yang, Ultrastable g-C_3N_4 assemblies with high quantum yield and reversible photoluminescence, Chem. Commun. 54 (2018) 13519–13522, https://doi.org/10.1039/C8CC07833E.
[4] K. Maeda, F. Takeiri, G. Kobayashi, S. Matsuishi, H. Ogino, S. Ida, T. Mori, Y. Uchimoto, S. Tanabe, T. Hasegawa, N. Imanaka, H. Kageyama, Recent progress on mixed-anion materials for energy applications, Bull. Chem. Soc. Jpn. 95 (2022) 26-37, https://doi:10.1246/bcsj.20210351.
[5] B.N. Bhadra, L.K. Shrestha, K. Ariga, Porous carbon nanoarchitectonics for the environment: detection and adsorption, CrystEngComm 24 (2022) 6804–6824, https://doi.org/10.1039/D2CE00872F.
[6] X. Wang, K. Maeda, A. Thomas, K. Takanabe, G. Xin, J. Carlsson, K. Domen, M. Antonietti, A metal-free polymeric photocatalyst for hydrogen production from water under visible light, Nat. Mater. 8 (2009) 76–80, https://doi.org/10.1038/nmat2317.

[7] X. Zhang, P. Yang, S.P. Jiang, Ni diffusion in vertical growth of MoS_2 nanosheets on carbon nanotubes towards highly efficient hydrogen evolution, Carbon 175 (2021) 176–186, https://doi.org/10.1016/j.carbon.2021.01.010.
[8] B. Shao, Z. Liu, G. Zeng, Z. Wu, Y. Liu, M. Cheng, M. Chen, Y. Liu, W. Zhang, H. Feng, Nitrogen-doped hollow mesoporous carbon spheres modified g-C_3N_4/Bi_2O_3 direct dual semiconductor photocatalytic system with enhanced antibiotics degradation under visible light, ACS Sustain. Chem. Eng. 6 (2018) 16424–16436, https://doi.org/10.1021/acssuschemeng.8b03480.
[9] K. Ariga, Nanoarchitectonics: what's coming next after nanotechnology, Nanoscale Horiz. 6 (2021) 364–378, https://doi.org/10.1039/D0NH00680G.
[10] X. Liu, F. He, Y. Lu, S. Wang, C. Zhao, S. Wang, X. Duan, H. Zhang, X. Zhao, H. Sun, J. Zhang, S. Wang, The double-edged effect of single atom metals on photocatalysis, Chem. Eng. J. 453 (2023), https://doi.org/10.1016/j.cej.2022.139833 139833.
[11] J. Li, S. Zhao, S. Yang, S. Wang, H. Sun, S. Jiang, B. Johannessen, S. Liu, Atomically dispersed cobalt on graphitic carbon nitride as a robust catalyst for selective oxidation of ethylbenzene by peroxymonosulfate, J. Mater. Chem. A 9 (2021) 3029–3035, https://doi.org/10.1039/D0TA11503G.
[12] X. Zhang, P. Wang, P. Yang, S.P. Jiang, Photo-chemical property evolution of superior thin g-C_3N_4 nanosheets with their crystallinity and Pt deposition, Inter. J. Hydrog. Energy 45 (2020) 21523–21531, https://doi.org/10.1016/j.ijhydene.2020.06.031.
[13] N.R. Glavin, R. Rao, V. Varshney, E. Bianco, A. Apte, A. Roy, E. Ringe, P.M. Ajayan, Emerging applications of elemental 2D materials, Adv. Mater. 32 (2020) 1904302, https://doi.org/10.1002/adma.201904302.
[14] A. Hayat, A.G. Al-Sehemi, K.S. El-Nasser, T.A. Taha, A.A. Al-Ghamdi, J.A.S. Syed, M.A. Amin, T. Ali, T. Bashir, A. Palamanit, J. Khan, W.I. Nawawi, Graphitic carbon nitride (g-C_3N_4)-based semiconductor as a beneficial candidate in photocatalysis diversity, Inter. J. Hydrog Energy 47 (2022) 5142–5191, https://doi.org/10.1016/j.ijhydene.2021.11.133.
[15] X. Zhang, S. He, S.P. Jiang, WO_x/g-C_3N_4 layered heterostructures with controlled crystallinity towards superior photocatalytic degradation and H_2 generation, Carbon 156 (2020) 488–498, https://doi.org/10.1016/j.carbon.2019.09.083.
[16] M.B. Zakaria, C. Li, Q. Ji, B. Jiang, S. Tominaka, Y. Ide, J.P. Hill, K. Ariga, Y. Yamauchi, Self-construction from 2D to 3D: one-pot layer-by-layer assembly of graphene oxide sheets held together by coordination polymers, Angew. Chem. Int. Ed. 55 (2016) 8426–8430, https://doi.org/10.1002/anie.201603223.
[17] N. Roy, N. Suzuki, C. Terashima, A. Fujishima, Recent Improvements in the Production of Solar Fuels: From CO_2 Reduction to Water Splitting and Artificial Photosynthesis, Bull. Chem. Soc. Jpn. 92 (2019) 178–192, https://doi.org/10.1246/bcsj.20180250.
[18] C.N.R. Rao, K. Pramoda, Borocarbonitrides, $B_xC_yN_z$, 2D nanocomposites with novel properties, Bull. Chem. Soc. Jpn. 92 (2019) 441–468, https://doi.org/10.1246/bcsj.20180335.
[19] K. Maeda, T.E. Mallouk, Two-dimensional metal oxide nanosheets as building blocks for artificial photosynthetic assemblies, Bull. Chem. Soc. Jpn. 92 (2019) 38–54, https://doi.org/10.1246/bcsj.20180258.
[20] X. Zhang, P. Yang, S.P. Jiang, Pt nanoparticles embedded spine-like g-C_3N_4 nanostructures with superior photocatalytic activity for H_2 generation and CO_2 reduction, Nanotechnology 32 (2021), https://doi.org/10.1088/1361-6528/abdcee 175401.
[21] X. Zhang, J.P. Veder, S. He, S.P. Jiang, Construction of 2D g-C_3N_4 lateral-like homostructures and their photo- and electro-catalytic activities, Chem. Commun. 55 (2019) 1233–1236, https://doi.org/10.1039/C8CC09633C.
[22] A.H. Asif, N. Rafique, R.A.K. Hirani, L. Shi, S. Zhang, S. Wang, H. Sun, Graphitic carbon nitride engineered α-Fe_2O_3/rGO heterostructure for visible-light-driven photochemical oxidation of sulfamethoxazole, Chem. Eng. J. 451 (2023), https://doi.org/10.1016/j.cej.2022.138630 138630.
[23] Y. Zhu, Z. Xu, Q. Lang, W. Jiang, Q. Yin, S. Zhong, S. Bai, Grain boundary engineered metal nanowire cocatalysts for enhanced photocatalytic reduction of carbon dioxide, Appl. Catal. B Environ. 206 (2017) 282–292, https://doi.org/10.1016/j.apcatb.2017.01.035.
[24] X. Zhang, X. Zhang, P. Yang, S.P. Jiang, Transition metals decorated g-C_3N_4/*N*-doped carbon nanotube catalysts for water splitting: A review, J. Electroanal. Chem. 895 (2021), https://doi.org/10.1016/j.jelechem.2021.115510 115510.
[25] X. Zhang, P. Yang, S.P. Jiang, The edge-epitaxial growth of yellow g-C_3N_4 on red g-C_3N_4 nanosheets with superior photocatalytic activities, Chem. Commun. 57 (2021) 3119–3122, https://doi.org/10.1039/D1CC00209K.
[26] S. Wang, J. Zhang, B. Li, H. Sun, S. Wang, Engineered graphitic carbon nitride-based photocatalysts for visible-light-driven water splitting: a review, Energy Fuels 35 (2021) 6504–6526, https://doi.org/10.1021/acs.energyfuels.1c00503.
[27] Z. Jiang, X. Zhang, H.S. Chen, P. Yang, S.P. Jiang, Fusiform-shaped g-C_3N_4 capsules with superior photocatalytic activity, Small 16 (2020) 2003910, https://doi.org/10.1002/smll.202003910.
[28] L. Lin, Z. Yu, X. Wang, Crystalline carbon nitride semiconductors for photocatalytic water splitting, Angew. Chem. Int. Ed. 58 (2019) 6164–6175, https://doi.org/10.1002/anie.201809897.
[29] Z. Jiang, C. Jia, B. Wang, P. Yang, G. Gao, Hexagonal g-C_3N_4 nanotubes with Pt decorated surface towards enhanced photo- and electro-chemistry performance, J. Alloys Compd. 826 (2020), https://doi.org/10.1016/j.jallcom.2020.154145 154145.
[30] X. Cai, A. Wang, J. Wang, R. Wang, S. Zhong, Y. Zhao, L. Wu, J. Chen, S. Bai, Order engineering on the lattice of intermetallic PdCu co-catalysts for boosting the photocatalytic conversion of CO_2 into CH_4, J. Mater. Chem. A 6 (2018) 17444–17456, https://doi.org/10.1039/C8TA06204H.
[31] Z. Sun, T. Ma, H. Tao, Q. Fan, B. Han, Fundamentals and challenges of electrochemical CO_2 reduction using two-dimensional materials, Chem. 3 (2017) 560–587, https://doi.org/10.1016/j.chempr.2017.09.009.
[32] V. Kumaravel, J. Bartlett, S.C. Pillai, Photoelectrochemical conversion of carbon dioxide (CO_2) into fuels and value-added products, ACS Energy Lett. 5 (2020) 486–519, https://doi.org/10.1021/acsenergylett.9b02585.
[33] Z. Jiang, X. Zhang, H.S. Chen, X. Hu, P. Yang, Formation of g-C_3N_4 Nanotubes towards superior photocatalysis performance, ChemCatChem 11 (2019) 4558–4567, https://doi.org/10.1002/cctc.201901038.
[34] J. Lin, W. Tian, H. Zhang, X. Duan, H. Sun, S. Wang, Graphitic carbon nitride-based Z-scheme structure for photocatalytic CO_2 reduction, Energy Fuels 35 (2021) 7–24, https://doi.org/10.1021/acs.energyfuels.0c03048.
[35] K. Zhu, X. Luan, K. Matras-Postolek, P. Yang, 2D/2D MoS_2/g-C_3N_4 layered heterojunctions with enhanced interfacial electron coupling effect, J. Electroanal. Chem. 893 (2021), https://doi.org/10.1016/j.jelechem.2021.115350 115350.
[36] T. Song, X. Zhang, P. Yang, Bifunctional nitrogen-doped carbon dots in g-C_3N_4/WO_x heterojunction for enhanced photocatalytic water-splitting performance, Langmuir 37 (2021) 4236–4247, https://doi.org/10.1021/acs.langmuir.1c00210.
[37] X. Li, W. Bi, L. Zhang, S. Tao, W. Chu, Q. Zhang, Y. Luo, C. Wu, Xie, Single-atom Pt as co-catalyst for enhanced photocatalytic H_2 evolution, Adv. Mater. 28 (2016) 2427, https://doi.org/10.1002/adma.201505281.
[38] T. Song, C. Xie, K. Matras-Postolek, P. Yang, 2D layered g-C_3N_4/WO_3/WS_2 S-scheme heterojunctions with enhanced photochemical performance, J. Phys. Chem. C 125 (2021) 19382–19393, https://doi.org/10.1021/acs.jpcc.1c06753.
[39] X. Zhang, X. Zhang, P. Yang, S.P. Jiang, Pt clusters embedded in g-C_3N_4 nanosheets to form Z-scheme heterostructures with enhanced photochemical performance, Surf. Interf. 27 (2021), https://doi.org/10.1016/j.surfin.2021.101450 101450.
[40] G. Liao, C. Li, S. Liu, B. Fang, H. Yang, Emerging frontiers of Z-scheme photocatalytic systems, Trends Chem. 4 (2022) 111–127, https://doi.org/10.1016/j.trechm.2021.11.005.
[41] S. Huang, Y. Long, S. Ruan, Y. Zeng, Enhanced photocatalytic CO_2 reduction in defect-engineered Z-scheme WO_{3-x}/g-C_3N_4 heterostructures, ACS Omega 4 (2019) 15593–15599, https://doi.org/10.1021/acsomega.9b01969.
[42] X. Zhang, X. Zhang, P. Yang, S.P. Jiang, Layered graphitic carbon nitride: nano-heterostructures, photo/electro-chemical performance and trends, J. Nanostr. Chem. 12 (2022) 669–691, https://doi.org/10.1007/s40097-021-00442-5.
[43] J. Sun, Y. Fu, G. He, X. Sun, X. Wang, Green Suzuki-Miyaura coupling reaction catalyzed by palladium nanoparticles supported on graphitic carbon nitride, Appl. Catal. B Environ. 165 (2015) 661–667, https://doi.org/10.1016/j.apcatb.2014.10.072.
[44] O.A. Baturina, Q. Lu, M.A. Padilla, L. Xin, W. Li, A. Serov, K. Artyushkova, P. Atanassov, F. Xu, A. Epshteyn, T. Brintlinger, M. Schuette, G.E. Collins, CO_2 electroreduction to hydrocarbons on carbon-supported Cu nanoparticles, ACS Catal. 4 (2014) 3682–3695, https://doi.org/10.1021/cs500537y.
[45] S. Bai, Q. Shao, P. Wang, Q. Dai, X. Wang, X. Huang, Highly active and selective hydrogenation of CO_2 to ethanol by ordered Pd-Cu nanoparticles, J. Am. Chem. Soc. 139 (2017) 6827–6830, https://doi.org/10.1021/jacs.7b03101.
[46] Z. Guo, Y. Xie, J. Xiao, Z.J. Zhao, Y. Wang, Z. Xu, Y. Zhang, L. Yin, H. Cao, J. Gong, Single-atom Mn–N_4 site-catalyzed peroxone reaction for the efficient production of hydroxyl radicals in an acidic solution, J. Am. Chem. Soc. 141 (2019) 12005–12010, https://doi.org/10.1021/jacs.9b04569.
[47] X. Wang, G. Hai, B. Li, Q. Luan, W. Dong, G. Wang, Construction of dual-Z-scheme WS_2-WO_3·H_2O/g-C_3N_4 catalyst for photocatalytic H_2 evolution under visible light, Chem. Eng. J. 426 (2021), https://doi.org/10.1016/j.cej.2021.130822 130822.
[48] C. Jia, X. Zhang, K. Matras-Postolek, B. Huang, P. Yang, Z-scheme reduced graphene oxide/TiO_2-Bronze/$W_{18}O_{49}$ ternary heterostructure towards efficient full solar-spectrum photocatalysis, Carbon 139 (2018) 415–426, https://doi.org/10.1016/j.carbon.2018.07.024.
[49] M. Liu, S. Wageh, A.A. Al-Ghamdi, Pe. Xia, B. Cheng, L. Zhang, J. Yu, Quenching induced hierarchical 3D porous g-C_3N_4 with enhanced photocatalytic CO_2 reduction activity, Chem. Commun.55 (2019) 14023-14026. 10.1039/C9CC07647F.
[50] Z. Liu, X. Zhang, Z. Jiang, H.S. Chen, P. Yang, Phosphorus and sulphur co-doping of g-C_3N_4 nanotubes with tunable architectures for superior photocatalytic H_2 evolution, Inter. J. Hydrog Energy 44 (2019) 20042–20055, https://doi.org/10.1016/j.ijhydene.2019.06.037.
[51] J. Lin, W. Tian, H. Zhang, X. Duan, H. Sun, H. Wang, Y. Fang, Y. Huang, S. Wang, Carbon nitride-based Z-scheme heterojunctions for solar-driven advanced oxidation processes, J. Hazard. Mater. 434 (2022), https://doi.org/10.1016/j.jhazmat.2022.128866 128866.
[52] H. Zhang, W. Tian, J. Zhang, X. Duan, S. Liu, H. Sun, S. Wang, Carbon nitride-based Z-scheme photocatalysts for non-sacrificial overall water splitting, Mater. Today Energy 23 (2022), https://doi.org/10.1016/j.mtener.2021.100915 100915.